Flowfield Analysis of a Small Entry Probe (SPRITE) Tested in an Arc Jet

Dinesh K. Prabhu[1]
ERC Inc., NASA Ames Research Center, Moffett Field, CA 94035

I. Introduction

A novel concept of small size (diameter less than 15 inches) entry probes named SPRITE (Small Probe Re-entry Investigation for TPS Engineering) has been developed at NASA Ames Research Center (ARC). These flight probes have on-board data acquisition systems that have also been developed in parallel at NASA ARC by Greg Swanson[1]. Flight probes of this size facilitate testing over a wide range of conditions in arc jets available at NASA ARC, thereby fulfilling a 'test what you fly' paradigm. As indicated by the acronym, these probes, with suitably tailored trajectories, are primarily meant to be robotic flight test beds for TPS materials, although the design is flexible enough to accommodate additional objectives of flight-testing other vehicle subsystems.

A first step towards establishing the feasibility of the SPRITE concept is to arc-jet test fully instrumented models at flight scale. In a follow-on to the Large-Scale Article Tests (LSAT[2]) performed in the 60 MW Interaction Heating Facility (IHF) in late 2008/early 2009, a full-scale model of Deep Space-2 (DS2[3]) made of red oak was tested in the 20 MW Aerodynamic Heating Facility (AHF). There were no issues with mass capture by the diffuser for blunt bodies of roughly 15 inches diameter tested in the 18-inch nozzle of the AHF. Building on this initial success, two identical test articles – SPRITE-T1-1 and SPRITE-T1-2 (T1 indicating the choice of back shell geometry) – were fabricated, and one of them, SPRITE-T1-1, was tested in the AHF recently. Both these test articles, 14 inches in diameter, have a 45° sphere-cone (like DS2) made of PICA bonded on to a 1/8th inch thick aluminum shell using RTV. The aft portion of the test article is a conical frustum (15° cone angle) with LI-2200 bonded on to the aluminum shell. Each model is fully instrumented with: (a) thermocouples imbedded in plugs in the heat shield, (b) thermocouples bonded to the aluminum substructure; the thermocouples are distributed over the entire shell, and (c) a few strain gages. Data from some of the thermocouples and gages are acquired by the on-board data acquisition system (DAS), while data from the others are routed to the facility-provided DAS, thereby enabling a cross check on the in situ measurement capability.

The two primary objectives of the arc-jet test AHF 295 were:

1. To demonstrate the feasibility of arc-jet testing flight articles at full scale – a required first step in the 'test what you fly' paradigm;
2. To demonstrate the feasibility of *in situ* measurements of temperature, strain and recession using a data acquisition system mounted inside the test article, i.e., to demonstrate gathering and storage of data acquired by sensors during an arc jet test.

A secondary objective of the test was to demonstrate the ability of a combination of simulation tools – primarily *DPLR*[4], *FIAT*[5], and *MARC*[6] – in predicting material response and thermal environments in the interior of the test article during arc jet testing.

II. Test Geometry

The test geometry is a 45° sphere-cone of 14 inches base diameter (*i.e.*, R_b = 14 in). The geometry is shown in a nozzle exit plane (NEP) centered coordinate system in Fig. 1. The nose radius, R_n, is 4 inches, and the radii of the two shoulders, R_s and R_c (fore and aft), are 0.4 and 0.25 inch, respectively. The conical frustum of the aft shell has a 15° inclination to the horizontal, and the total axial length, L_b, of the test article is 11 inches. Also shown in Fig. 1 are the locations of the instrumented plugs used in the test. The locations of the plugs are approximate and measured from the tangency point of the front conical frustum and the shoulder torus. For the purpose of CFD analysis, which is to provide the initial heat flux on the test article, only the outer mold line (OML) of the test article matters; the time-varying distribution of heat through the thickness of the materials that make up the test article is determined by a materials thermal response code.

[1] Senior Research Scientist, Aerothermodynamics Branch, Mail Stop 230-3. Associate Fellow AIAA.

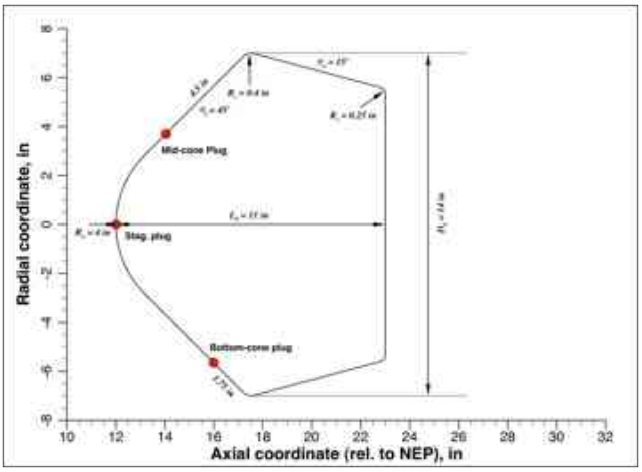

Figure 1. SPRITE-T1 geometry tested in the 18-inch nozzle of the 20 MW Aerodynamic Heating Facility (AHF).

III. Test Conditions and Calorimetry

The test entry AHF 295 consisted of multiple insertions of calorimeters (for calibration) and one test of SPRITE-T1 at a single arc heater setting – close to the maximum condition that could be achieved in the facility. All tests were conducted in the 18-inch nozzle of the AHF, with calorimeters/test article placed at 12 inches from the NEP. The flow rates of the main air, add air, and argon (electrode shield gas) streams were selected to be, 321, 31, and 36 gm/s, respectively, and maintained for all runs of the test entry. The arc current was set to the nominal maximum of the facility at 2000 A, with a slight run-to-run variability occurring in the potential drop across the arc, and consequently the pressure developed by the arc column.

Although traditionally a calorimeter of the same shape and size as the test article is used to provide calibration via cold-wall heat flux and pressure measurements, such a step was dispensed with in AHF 295 – cost and lead time in the fabrication of a calorimeter being the primary considerations in a program conducted almost entirely on goodwill within the Entry Systems and Technology Division at NASA Ames Research Center. Instead, a number of different (in shape and size) calorimeters – 4-inch hemispherical, 4-in iso-q (a workhorse in several programs, notably the CEV program), and flat-faced cylindrical (4- and 6-inch diameter) calorimeters – were used in the tests. For all calorimeters, stagnation point heat flux and pressure measurements were made, and using a 6-inch flat-faced calorimeter with distributed slugs, off-stagnation heat flux measurements were also taken. The distributed slugs also made it possible to obtain some assessment of flow asymmetry. The test article and all calorimeters were deployed at a distance of 12 inches from the NEP. Table 1 summarizes the results of measurements, along with the values of key arc heater parameters.

Table 1. Summary of calometric measurements in AHF 295 (facility max conditions)

Date	Run #	Arc Current	Arc Voltage	Column Pressure	Bulk enthalpy	Calorimeter	Pressure	Heat Flux			
							Stag.	Stag.	Inner1/ Outer1	Outer2	Outer3
		A	V	kPa	MJ/kg		kPa	W/cm^2			
12/13	**1**	2023	5084	833	11.5 (13.5)	4in Iso-q	8.4	167.0			
						4in Iso-q	8.3	167.0			
12/14	**2**	2023	5116	837	11.6 (13.5)	4in Iso-q	8.4	171.0			
						4in Iso-q	8.4	167.0			
						4in Hemi	8.1	220.0			
						6in FF (IL)[a]	8.4	113.0	113.0	119.0	
						6in FF (T)[b]	8.5	98.0	124.0	109.0	124.0
12/15	**3**	2010	5146	837	11.5	4in Iso-q	8.4	170.0			
						4in Iso-q	8.4	165.0			
12/16	**59**[c]	2014	5158	844	11.1 (12.7)	4in FF	8.3	123.0			
						4in Hemi[d]	8.3	224.0			

[a] Inline slugs – one slug 1 inch from the center, and the second 2 inches from the center
[b] Three outer slugs at the corners of an equilateral triangle circumscribed by a circle of radius 2 inches
[c] Part of AHF 999 calibration series – data provided as a courtesy
[d] Different calorimeter than the one used in Run 2
Old estimates of bulk enthalpy are shown in parentheses. EB2 values were revised on Jan. 3, 2011 by Imelda Terrazas-Salinas (ARC/TSF)

The centerline enthalpy can be inferred from the stagnation point measurements of pressure and cold-wall heat flux by inverting a simplified version of the Fay-Riddell correlation[8]:

$$H_{CL} \approx \frac{1}{K}\frac{\sqrt{R_{\text{eff}}}}{\sqrt{p_{\text{stag}}}} q_{\text{stag}} \qquad K = \left(\frac{c_{\text{Air}}}{K_{\text{Air}}} + \frac{c_{\text{Ar}}}{K_{\text{Ar}}}\right)^{-1} \qquad c_{Air} = \frac{m_{Air} + m_{Air+}}{m_{Air} + m_{Air+} + m_{Ar}} \qquad c_{Ar} = 1 - c_{Air} \tag{1}$$

where m_{Air}, m_{Air+}, and m_{Ar}, are respectively, the flow rates of air, add air, and argon, and the constants K_{Air} and K_{Ar} have values, 3.904×10^{-4} and 5.513×10^{-4} kg/m$^{3/2}$.s.$\sqrt{\text{atm}}$[9], respectively. Note: it is assumed that the 'effective radius', R_{eff}, of a non-hemispherical calorimeter is known either a priori (using the work of Zoby and Sullivan[10]) or using measured data from a hemispherical calorimeter of known radius, R_{hemi}:

$$R_{\text{cal}} = R_{\text{hemi}}\left(\frac{q_{\text{hemi}}}{q_{\text{cal}}}\right)^2 \tag{2}$$

The centerline enthalpy values and effective radii obtained by applying Eqs. 1 and 2 to the data shown presented in Table 1 are given in Table 2. Other than the data obtained from the 6-inch flat-face calorimeter with inline slugs, there is very good consistency in the measurements. The effective radius, computed using the 4-inch hemispherical calorimeter as the reference (Eq. 2), of each non-hemispherical calorimeter is in very good agreement (less than ±5% difference) with that obtained from the work of Zoby and Sullivan[10]. As a consequence, there is very good consistency in estimates of centerline enthalpy using Eq. 1 – an average of 13.7 MJ/kg is obtained from all calorimetric measurements. This average value of 13.7 MJ/kg for centerline enthalpy compares favorably with the bulk enthalpy measured using energy balance (EB2)[10] in Runs 1 and 2, suggesting uniformity in flow profiles at the nozzle inlet. The EB2 values of Runs 3 and 4 are inexplicably smaller (by 6-17%) than in Runs 1 and 2. This discrepancy in EB2 measurements remains to be investigated further.

Table 2. Centerline enthalpy and effective radius estimates from measurements

Date	Run #	Calorimeter	Effective radius[a] in	p_{stag} kPa	q_{stag} W/cm^2	Centerline enthalpy MJ/kg	Effective radius[b] in
12/13	**1**	4in Iso-q	3.57	8.4	167.0	13.7	
		4in Iso-q	3.57	8.3	167.0	13.7	
12/14	**2**	4in Iso-q	3.57	8.4	171.0	14.0	3.31
		4in Iso-q	3.57	8.4	167.0	13.7	3.39
		4in Hemi	2.00	8.1	220.0	13.7	
		6in FF (IL)[a]	10.00	8.4	113.0	15.5	3.79
		6in FF (T)[b]	10.00	8.5	98.0	13.3	10.08
12/15	**3**	4in Iso-q	3.57	8.4	170.0	13.9	
		4in Iso-q	3.57	8.4	165.0	13.5	
12/16	**4**	4in FF	6.35	8.3	123.0	13.5	6.632
		4in Hemi[c]	2.00	8.3	224.0	13.8	

[a] Effective radius using Zoby-Sullivan chart
[b] Effective radius using measured heat flux on a 4-in hemispherical calorimeter
[c] Different calorimeter than the one used in Run 2

If an estimate of bulk enthalpy by energy balance is not available, a work around is to estimate the bulk enthalpy using correlations based on the idea of sonic flow at the nozzle throat (choked flow) and isentropic flow in the plenum. These correlations are of the form:

$$H_{\text{bulk}} = \left(\frac{C}{\sigma}\right)^{\phi} \qquad \sigma = \frac{m}{A_{\text{throat}} P_{\text{arc}}} \tag{3}$$

where C and ϕ are constants, A_{throat} is the cross sectional area of the nozzle throat, and P_{arc} is the pressure developed in the arc column. In the correlation of Winovich[12], C = 123 and ϕ = 2.519, while in the correlation of Shepard et al.[13], C = 158.7 and ϕ = 1.971. Based on dimensional considerations and a significant amount of data gathered over the last decade, Thompson et al.[14] have recently revised the correlation with C = 155.8 and ϕ = 2. This correlation with the values of Thompson et al., when applied to the test conditions shown in Table 1, provides bulk enthalpy estimates shown in Table 3.

Table 3. Bulk enthalpy estimates

Date	Run #	Sonic Flow Parameter (s) s/m	$H_{bulk,fit}$ MJ/kg
12/13	1	41.29	14.24
12/14	2	41.09	14.38
12/15	3	41.09	14.38
12/16	4	40.86	14.54

The arithmetic average of the theoretical estimates of bulk enthalpy is 14.385 MJ/kg, which is about 6.6% higher than the EB2 (measured) value of 13.5 MJ/kg. The influence of this uncertainty in bulk enthalpy can be assessed in the material thermal response computations.

IV. Computational Analysis and Results

A complete set of experimental data is now available for use in simulation of the flow field that develops in the nozzle and over the test article. A strategy adopted in the present work is to use the axisymmetric simulation methodology developed by Prabhu et al.[15] The simulation procedure was originally developed around v3.05 of the in-house flow solver, *DPLR*, and one of the objectives of the present work is to upgrade the procedure with the latest version, v4.02.1,[4] which offers a more stable option of a subsonic inflow boundary condition based on the method of characteristics. Detailed flow computations are performed first for the various calorimeters used in the test (AHF 295). Once the flow solver is calibrated to calorimetric measurements (pressure and heat flux), detailed computations are performed for the test article. The resulting heat flux and pressure are then provided as inputs to v2.6.1 of the in-house materials thermal response code, *FIAT*.[5]

A. Flowfield Simulations

The bulk enthalpy and total flow rate (along with mass fractions of N_2, O_2, and Ar) of the test are provided as inputs to a code called *NOZZLE_THROAT_CONDITIONS*. This code, developed in-house by Gökçen and Saunders,[16] uses the *CEA* code (formerly called the Gordon-McBride code)[17] as the computational engine; the thermochemical state of the arc-heated gas mixture can be assumed to be thermodynamic equilibrium on account of high pressure (> 1 atm) in the arc column. The resulting mixture mass density, velocity (obtained from the speed of sound and assumed Mach number), temperature, and mass fractions of the constituent species (N_2, O_2, NO, N, O, and Ar) are used as pointwise BC inputs to *DPLR*. The computational domain consists of the entire convergent-divergent nozzle and the free jet in which a calorimeter or test article is inserted. The computational boundaries for the free jet (plus calorimeter) are truncated so that a supersonic extrapolation boundary condition can be applied to them. Further, the water-cooled nozzle wall and the surface of the copper calorimeter are assumed to be at a constant temperature of 400 K (127 °C), and fully catalytic to atom recombination.

B. Simulations of Calorimeters: Round 1, *DPLR* v3.05

In the first round of simulations, only calorimeters are considered. Computational grids for the calorimeter geometries of AHF 295 had already been created and tested in pre-test computations. The grid block corresponding to each of the calorimeters was adapted to the bow shock, and the wall-normal spacing controlled so as to achieve a cell Reynolds number of O(1) over the calorimeter. The in-house code SAGE[18] was used for the grid adaption.

The computed values of pressure and cold-wall heat flux at the stagnation point of each calorimeter are given in Table 4. Also shown in the table are the effective radii of each non-hemispherical calorimeter, using the 4-inch hemispherical calorimeter as the reference.

Table 4. Computational predictions of pressure and cold-wall heat flux at the stagnation point using DPLR v3.05

Calorimeter	Experiment[a]			CFD (DPLR v3.05), H_{bulk} = 13.7 MJ/kg				
	p_{stag} kPa	q_{stag} W/cm^2	R_{eff} in	p_{stag} kPa	q_{stag} W/cm^2	Diff. from expt. Pressure	Diff. from expt. Heat flux	R_{eff} in
4in Hemi	8.28	222.0		7.99	264.9	-3.5%	+19.3%	
4in Iso-q	8.38	167.8	3.501	8.08	190.1	-3.6%	+13.3%	3.884
4in Flat Face	8.30	123.0	6.515	8.14	129.5	-1.9%	+5.3%	8.369
6in Flat Face[b]	8.50	98.0	10.263	8.26	102.7	-2.8%	+4.8%	13.306

[a]Arithmetic average of all measurements
[b]Results for center slug only

Although the agreement between computation and experiment is excellent for the flat-faced calorimeters, the disagreement for the calorimeters with surface curvature is unacceptably high. This disagreement is even more disconcerting given that the experimental data appear to be internally consistent – they all yield nearly similar values for centerline enthalpy, and the effective radius computed for each non-hemispherical calorimeter using the hemispherical one as the reference.

Additional computations were performed for the hemispherical and iso-q calorimeters with flat-faced slugs of 0.38-inch diameter, i.e., exposed faces of the copper slugs at the stagnation point were assumed to have zero curvature. The pressure and heat flux distributions for the 4 calorimeters – hemispherical, iso-q, and flat-face cylindrical – are shown in Fig. 2. Also shown (as dashed lines) are the distributions for the hemisphere and iso-q calorimeter with flat-faced slugs. Clearly, the assumption of curvature mismatch, as in flat-face slug in a spherical section, does not help improve the accuracy of predictions. At best, the assumption of a flat-faced slug decreases the predicted heat flux by about 5%. The error bars shown in the figure are somewhat arbitrary in that they do not represent actual measurement errors, and are based on claims/estimates provided by experienced arc jet test engineers. They are only meant to provide a relative measure of calorimeter performance.

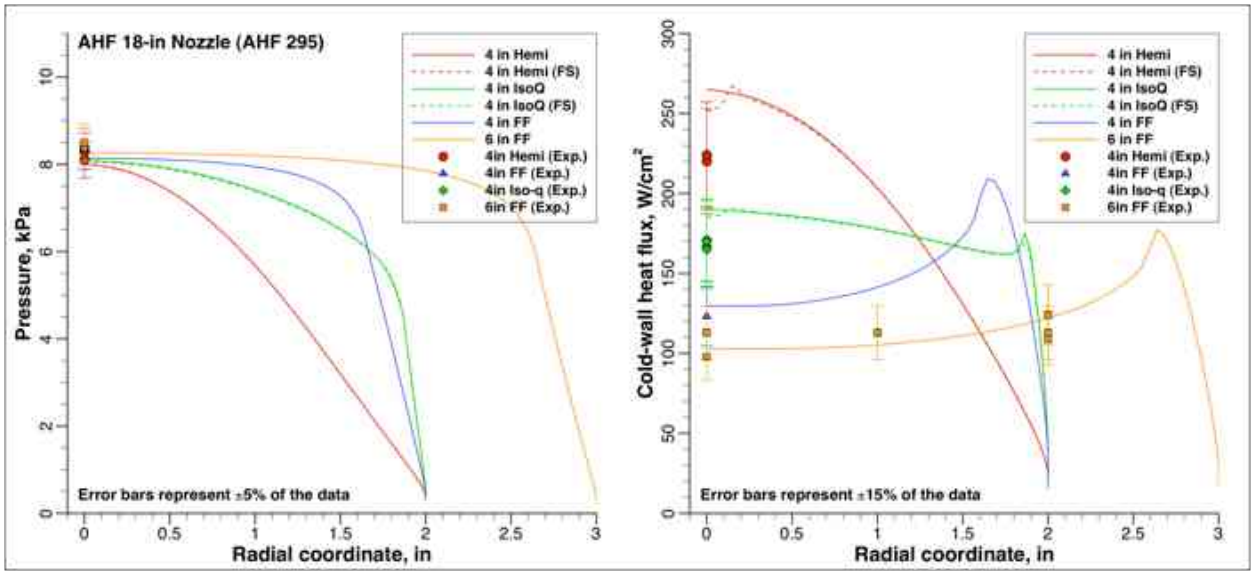

Figure 2. Pressure and cold-wall heat flux distributions over various calorimeters employed in AHF 295. The symbols represent experimental data, but the error bars shown are assumed measures of performance of calorimeter, and meant to provide a basis for discussion.

One is thus left with the uncomfortable situation of predictions in excellent agreement for some, but not all, calorimeters. Given the number of free parameters – inflow Mach number, wall temperature, surface catalysis, etc. – an attempt has been made to upgrade the simulation procedure to the latest version (v4.02.1) of DPLR, which has added new features. This is discussed next.

C. Simulations of Calorimeters: Round 1, *DPLR* v4.02.1

Version 4.02.1 of DPLR offers the new feature of being able to specify a stagnation pressure and temperature for a subsonic inflow boundary, and uses the method of characteristics in conjunction with the assumption of isentropic flow. This should be contrasted with the procedure adopted in v3.05, where an inflow Mach number was specified and the inflow boundary was considered to be fixed (invariant in time). The inflow Mach number was determined approximately, and the Dirichlet boundary condition specifies more than the number of requisite variables, which could result in non-conservation of mass.

As a first step towards handing off the process from v3.05 to v4.02.1 of DPLR, computations were performed for the 4-inch hemispherical calorimeter. The inflow conditions of v3.05 were used in v4.02.1, but the inflow Mach number was allowed to float. The resulting predictions of distributed surface temperature and cold-wall heat flux are shown in Fig. 3.

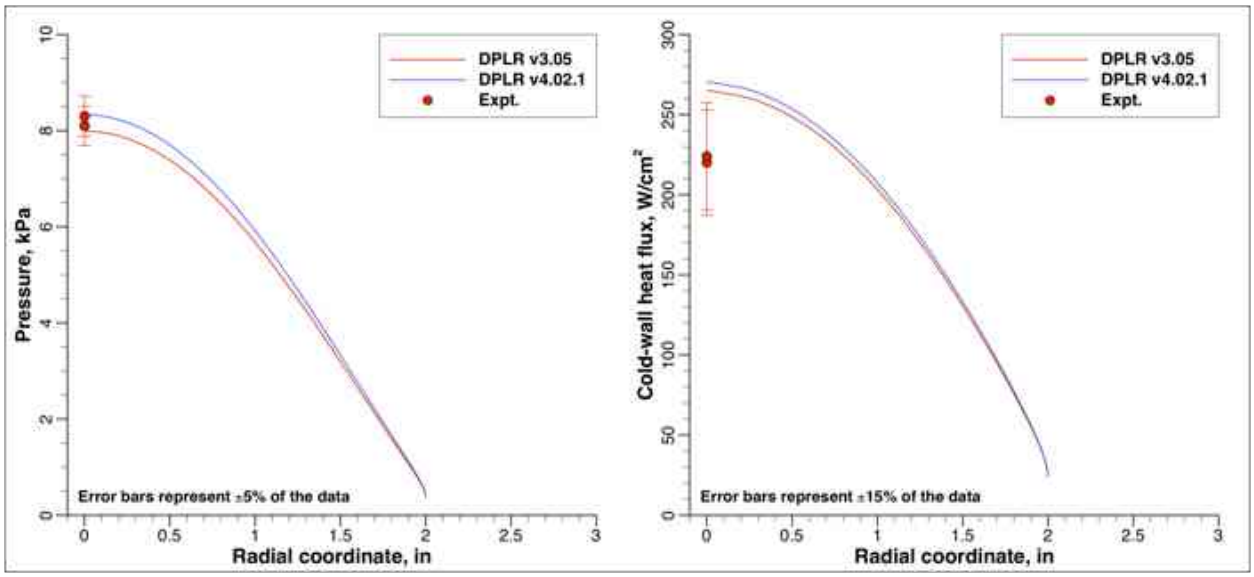

Figure 3. Pressure and cold-wall heat flux distributions, obtained using v3.05 and v4.02.1 of DPLR, over a 4-inch hemispherical calorimeter.

The preliminary conclusion from this one-off computation is that the agreement in predictions of v3.05 and v4.02.1 of DPLR is fair, but the reduction of one free parameter (inflow Mach number) in simulations is the primary motivator for wanting to switch to the newer version. In the simulation process based on v3.05 of DPLR, the inflow Mach number assumed at the nozzle inlet is usually 0.053 – based on simple application of gas dynamic equations while the subsonic inflow boundary condition used in v4.02.1 yields a value of 0.0538, which is 1.5% higher.

It should be noted that even with the elimination of the inflow Mach number as an uncertainty there is no improvement in the predicted level of heating at the stagnation point, and therefore another explanation should be sought. The surface temperature at the stagnation point of the test article (SPRITE-T1) was monitored using an IR camera and a pyrometer during Run 3 of AHF295. The time traces shown in Fig. 4 perhaps provide a clue.

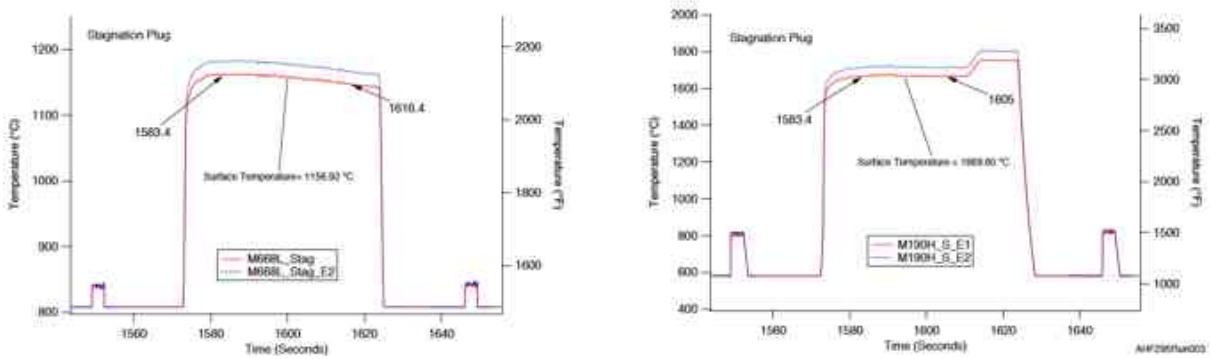

(a) IR Camera **(b) Pyrometer**

Figure 4. Time traces of surface temperature measured using: (a) an IR cameria, and (b) a one-color pyrometer during Run 3 of AHF 295.

Time traces of surface temperature of the test article are between t ≈ 1572 s to t≈1625 s (a period of roughly 50 s – the desired exposure time of the test), and are clearly seen in Fig. 4. The two smaller (and narrower) pulses on either side of the tall/broad pulse in Fig. 4 are the temperatures of the slugs of the 4-inch iso-q calorimeter inserted in the freestream before and after the exposure of the test article. The time traces are remarkably steady over the exposure times of the slug. From the pyrometer data, it can be inferred that the exposed face of the slug reached about 800 °C (1073 K) during the couple of seconds the calorimeter dwelled in the free jet, and that value was nearly a constant during the exposure. The value of approximately 840°C (1113 K) read by the IR camera differs from that read by the pyrometer, but that difference is not expected to impact heat computations performed with a temperature value of 1073 K, which is larger than the nominal value of 400 K assumed in cold-wall computations.

Computations were performed for three cases: (a) the baseline case in which both the nozzle wall and slug temperature are held at 400 K, (b) a modified case in which the nozzle wall is held at 400 K, but the slug temperature is held constant at 1073 K, and (c) a second modified case in which the nozzle wall is held at 300 K, and the slug temperature is held at 1073 K. In all three cases, the walls (both nozzle wall and calorimeter surface) in the computational domain are assumed fully catalytic to atom recombination, i.e., catalytic efficiency of the material is unity, even though the assumption of a fully catalytic wall at 1073 K is tenuous. Further, these computations are necessary because specification of the temperature of the slug as a single wall temperature for the entire calculation will alter the flow structure in the nozzle. A thicker boundary layer (as a consequence of increased wall temperature) that develops on the nozzle wall will set up a completely different wave interaction pattern, and influence the stagnation point pressure and the heat flux. One final important point to note here is that the temperature of the slug surface is imposed over the entire calorimeter holder. This is probably not true as the flow expands away from the stagnation point, but is adequate at this stage of the analysis. The pressure and heat flux distributions for the various cases are shown in Fig. 5.

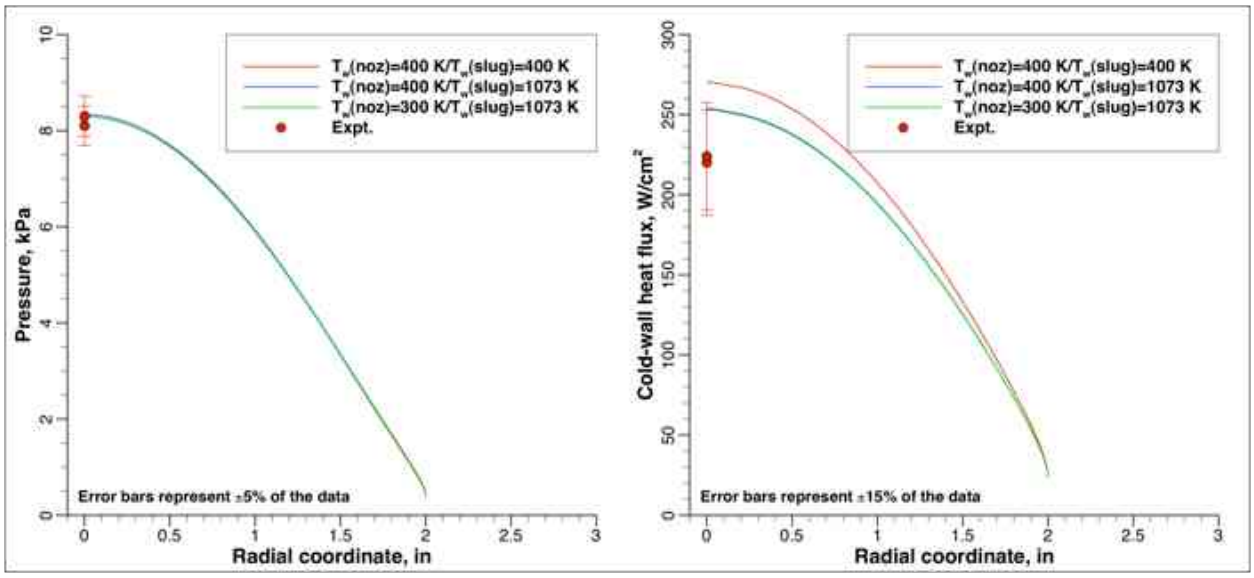

Figure 5. Influence of nozzle and slug temperature on stagnation point pressure and heat flux.

In Fig. 5, it is clearly seen that increased slug temperature results in lower heat flux, while the pressure remains unaffected. The decrease in heat flux is simply an indication of decreased enthalpy potential between the edge of the boundary layer and the wall. Although the predicted heat flux now falls within the assumed ±15% error bar, it is still in significant disagreement with measurement. Even the assumption of a flat-faced slug surface will not be sufficient to match the experimental data points.

The final degree of freedom in the computational model is the catalycity of copper. All results presented so far have assumed copper (material that makes up both the nozzle and the calorimeter) is fully catalytic to recombination of atoms. While this is a reasonable assumption to make if the wall is maintained at a sufficiently low temperature, it becomes increasingly tenuous as the wall temperature exceeds 1000 K. A sufficiently convincing model for gas-surface interaction does not exist currently. However, the research carried out by Barbato et al.[19] can be put to practical use. As per the reference cited, the efficiencies of copper in recombining nitrogen and oxygen atoms are 0.28 and 0.1, respectively. For a slug surface temperature of 1073 K (and nozzle wall at 400 K), additional computations are performed for a noncatalytic slug surface (a limiting case), and a partially catalytic surface with recombination efficiencies of Barbato et al. The computational predictions of surface pressure and heat flux are shown in Fig. 6.

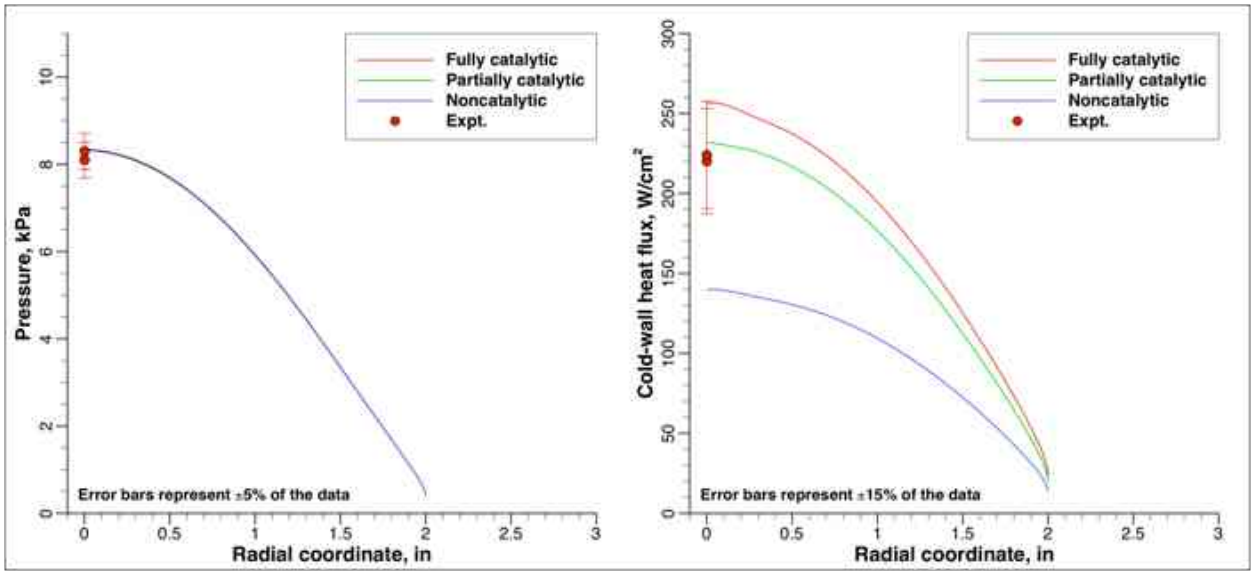

Figure 6. Influence of slug surface catalytic recombination efficiency on stagnation point pressure and heat flux.

The results shown in Fig. 6 indicate that copper is likely to be partially catalytic and definitely not non-catalytic. While the predicted pressure is relatively insensitive to the surface catalysis model employed, the heat flux for a partially catalytic wall, or a wall with a reduced catalytic efficiency to atom recombination, is in much better agreement with experiment – prediction is only 4.2% higher than experiment. It then remains to be seen if the assumption of a partially catalytic wall can replicate measured pressure and heat flux for all calorimeters used in AHF 295. The results of such computations are shown in Table 5. The lack of agreement in the 'theoretical' effective radius (i.e., effective radius inferred from CFD results) and that from the work of Zoby and Sullivan still remains to be investigated. It is likely that the boundary-layer edge conditions are different for the different calorimeters despite the fact that all of them were tested at the same distance from the nozzle exit plane; flow relaxation between shock and body depends on the shock standoff distance, which is the largest for the 6-inch flat-faced cylindrical calorimeter and the smallest for the hemispherical one.

Table 5. Computational predictions of pressure and cold-wall heat flux at the stagnation point using DPLR v4.02.1

Calorimeter	Experiment			CFD (DPLR v4.02.1), H_{bulk} = 13.7 MJ/kg				
	p_{stag} kPa	q_{stag} W/cm^2	R_{eff} in	p_{stag} kPa	q_{stag} W/cm^2	Diff. from expt. Pressure	Diff. from expt. Heat flux	R_{eff} in
4in Hemi	8.28	222.0		8.34	231.6	+0.7%	+4.2%	
4in Iso-q	8.38	167.8	3.501	8.43	169.1	+0.6%	+0.8%	3.752
4in Flat Face	8.30	123.0	6.515	8.49	117.6	+2.3%	-4.4%	7.757
6in Flat Face	8.50	98.0	10.263	8.62	94.1	+1.4%	-4.0%	12.115

The agreement between computation and experiment at the stagnation point is now excellent for all calorimeters. The pressure and heat flux distributions for the 4 calorimeters – hemispherical, iso-q, and flat-face cylindrical – are shown in Fig. 7.

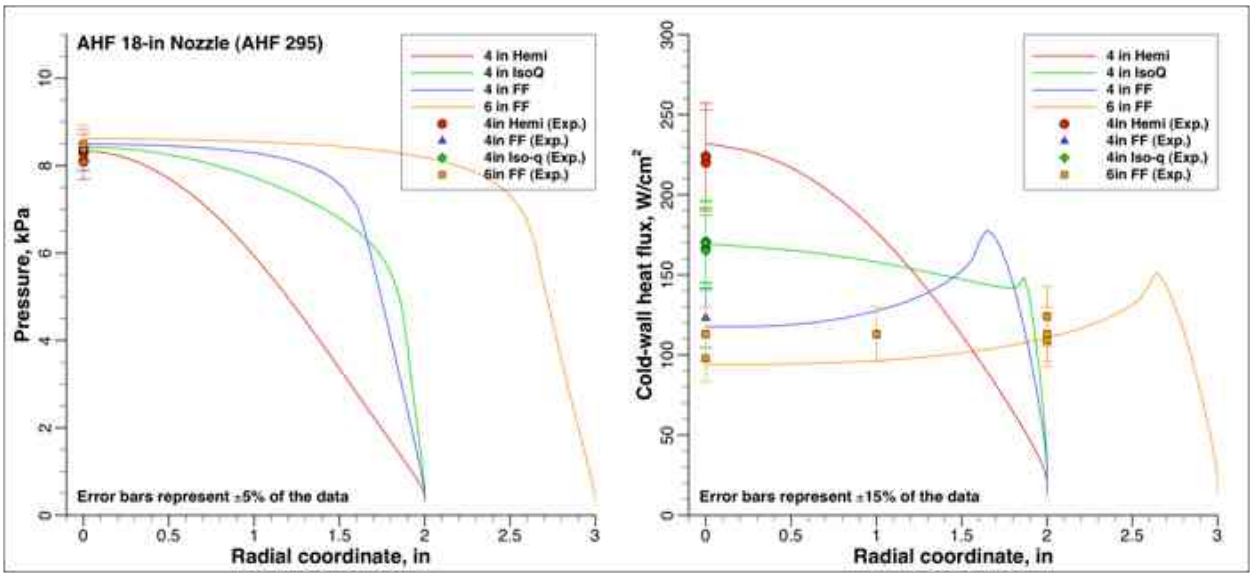

Figure 7. Pressure and cold-wall heat flux distributions over various calorimeters employed in AHF 295. Computations assume copper to be partially catalytic to atom recombination, and the calorimeter surface is set to a constant temperature of 1073 K (pyrometer measurement at the stagnation point).

The analysis presented thus far is a refinement over the CFD process built around v3.05 of DPLR. Although the analysis shows that it is quite plausible that copper is partially catalytic, further work and application to a larger number of test cases remains to be done. The good agreement between experiment and computations for this particular arc-heater setting for all calorimeters is particularly encouraging. The lessons learned from simulations of calorimeters are applied to the actual test article.

D. Test Article Simulation

Simulation of the flow field around the test article is straightforward. The only additional 'complexity' in the computation is inclusion of the entire test article (sans the sting to avoid a time-consuming 3D computation), and as a consequence, the diffuser as well. The inflow conditions are the same as those used in calorimeter simulations with v4.02.1 of *DPLR*. The assumption here is that the simulation procedure has been sufficiently calibrated against calorimetry, which is focused on the stagnation point alone. There are limited amount of off-stagnation measurements with a 6-inch flat-faced calorimeter. These data cover about 4 inches (diameter) of the core flow. Since the predicted heat flux at the off-stagnation locations are in good agreement with measurements, making some allowance for flow asymmetry, application of the conditions and procedures to the test article is likely going to be adequate.

Computations have been performed using v4.02.1 of *DPLR* for the test article. As with the calorimeters, computations have been performed three different ways: (a) the baseline method with nozzle, test article, and diffuser walls set to 400 K, and catalytic recombination efficiency set to unity, (b) the alternate method with the nozzle and diffuser walls set to 400 K, the test article surface set to 1073 K, and the catalytic recombination efficiencies (for N and O) set to values prescribed by the model of Barbato et al., and (c) the baseline hot wall method in which the nozzle and diffuser wall are assumed fully catalytic and set to a temperature of 400 K, and the test article is assumed fully catalytic to atom recombination, but with the ability to re-radiate heat with an emissivity of 0.85. It should be noted that the third model does not consider conduction of heat through the thickness of the material, i.e., an adiabatic back wall is tacitly assumed in the model.

The grid topology for these computations is not very amenable to grid tailoring or grid adaption, so no attempt is made here to adapt the grid to the bow shock and boundary layer. Since the bow shock will be misaligned with the grid, the heat flux, especially in the vicinity of the stagnation point, is expected to be a little less smooth. Furthermore, the computation does not include a sting, and the flow in the wake is likely to be unsteady (numerically) past the flow separation point on the aft shell.

In the absence of a calorimeter of the same shape and size as the test article, scaling arguments are relied upon to assess the accuracy of computations. Since the nose radius of the SPRITE-T1 geometry is 4-inches, the cold-wall heat flux should be roughly 41% lower than that for the hemisphere by a simple scaling argument based on the Fay-Riddell correlation. From Table 2, this works out to roughly 155-160 W/cm^2 – the upper estimate coming from the fact that the nose radius of the SPRITE-T1 geometry and that of the 4-inch iso-q calorimeter are very similar (3.57 vs 4.00 inches).

Distributions of surface pressure and heat flux obtained from the three computations mentioned above are shown in Fig. 8. Also shown are the predicted surface shear stresses and temperatures in Fig. 9.

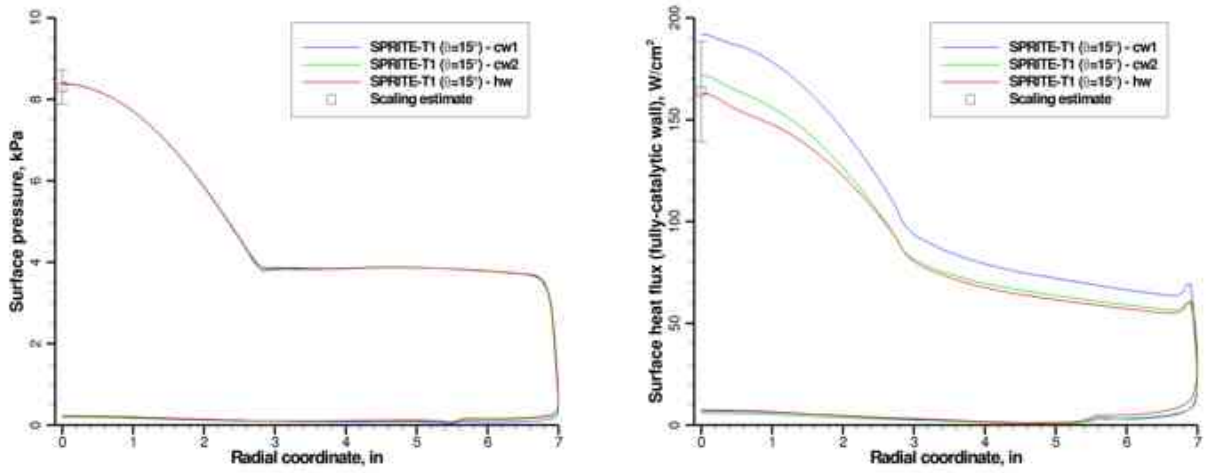

(a) Surface pressure **(b) Surface heat flux**

Figure 8. Pressure and heat flux (cold and hot wall) distributions over the SPRITE-T1 configuration tested in AHF 295. Results of computations in which all walls (nozzle, test article, and diffuser) are set to 400 K are designated by 'cw1' (blue curves) and computations in which the test article surface temperature is set to 1073 K, and the nozzle and diffuser walls set to 400 K are designated by 'cw2' (green curves). The hot-wall computations are designated by 'hw' (red curves).

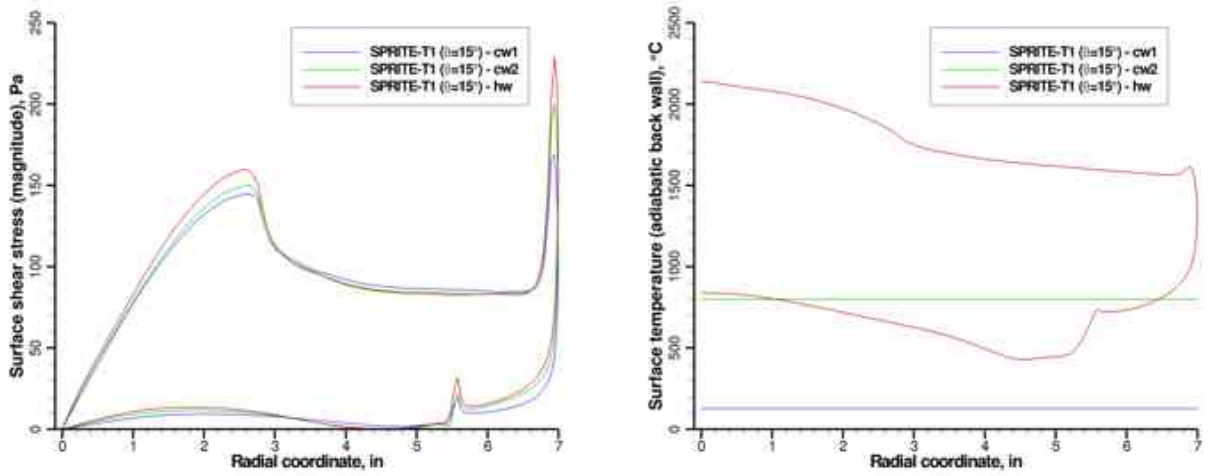

(a) Surface shear (magnitude) **(b) Surface temperature (adiabatic back wall)**

Figure 9. Shear stress and temperature distributions over the SPRITE-T1 configuration tested in AHF 295. Results of computations in which all walls (nozzle, test article, and diffuser) are set to 400 K (127 °C) are designated by 'cw1' (blue curves) and computations in which the test article surface temperature is set to 1073 K (800 °C), and the nozzle and diffuser walls set to 400 K (127 °C) are designated by 'cw2' (green curves). The hot-wall computations are designated by 'hw' (red curves).

The predicted radiation equilibrium temperatures (albeit with an adiabatic back wall) in the hot-wall computations are in excess of 2000 °C. At such temperatures, the assumption of a fully-catalytic wall is tenuous. However, it is assumed that the heat transfer coefficient, required in materials thermal response computations, is weakly dependent on wall temperature. Therefore, the results of the hot-wall computations for the SPRITE-T1 configuration are used in response computations

E. Materials Thermal Response Analysis

The computed flow field solution for the hot-wall case was post-processed using an in-house software utility, BLAYER, to extract boundary-layer properties – edge, wall, thickness, etc. The surface pressure, edge enthalpy, and convective heat transfer coefficient (film coefficient) were extracted at locations corresponding to the center of each instrumented plug (see Fig. 1). These quantities were provided as inputs to v2.6.1 of the materials thermal response code, FIAT. The stack up of the material on the heatshield was defined as PICA with 0.01 inch thick RTV-560 to bond the material to 0.125 thick Al-2024 (the structural shell). While the thickness of PICA is 1 inch over the conical frustum, it is about 1.36 inches thick at the stagnation point, because the aluminum shell had a flat face rather a curved one conforming to the nose radius of the OML. Each instrumented plug had 3 in-depth thermocouples (K type). The 2 plugs on the conical frustum had the thermocouples at nominal depths of 0.125, 0.375, and 0.625 inch, and for the stagnation point plug these depths were 0.25, 0.50, and 0.75 inch. The inputs used in FIAT computations are shown in Table 6. Computations were run out to 3600 seconds, which included 50 seconds of exposure of the test article to the arc-heated stream.

Table 6. Inputs to FIAT v2.6.1

Plug location	PICA thickness in	TTT fiber orientation	H BTU/lbm	$r_e u_e C_H$ lbm/ft^2.s	p atm
Stagnation point	1.36	0°	5869	0.0310	0.0828
Mid-cone	1.00	45°	5877	0.0126	0.0379
Bottom cone	1.00	45°	5878	0.0104	0.0377

Predicted time histories of surface temperature and thermocouple temperatures for the three plugs are shown in Fig. 10a-d. At the time of writing this report, experimental data were not available to make direct comparisons of predictions. However, the run summary sheets provided included experimental data represented graphically. It should be noted here that the materials response code has been run as a black box, and not too much effort has gone into fine-tuning any of the input parameters.

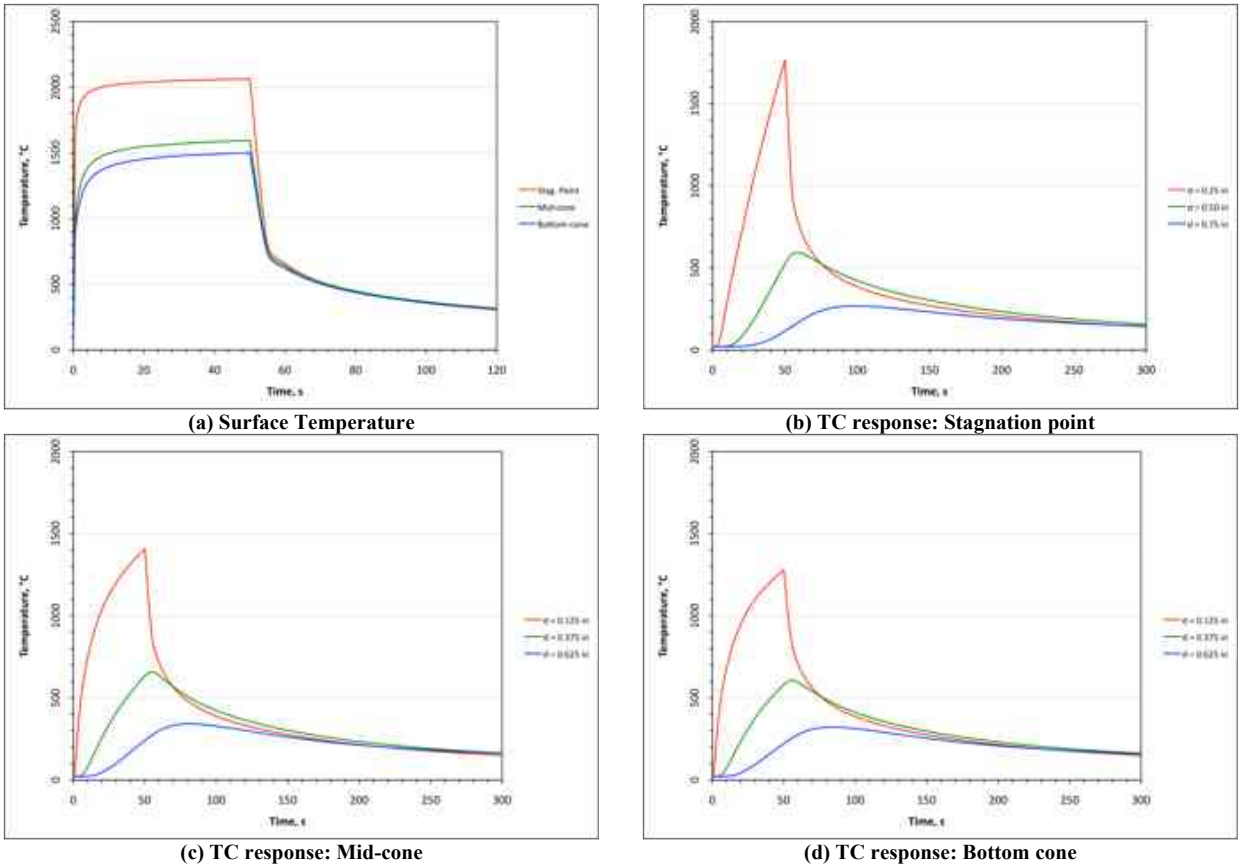

(a) Surface Temperature **(b) TC response: Stagnation point**

(c) TC response: Mid-cone **(d) TC response: Bottom cone**

Figure 10. Time histories of predicted temperatures (surface and in-depth) from application of FIAT v2.6.1 to results from flow field computations.

Reported values of temperature (from pyrometer measurements) are compared with predicted surface temperatures in Table 7. The large mismatch (≈20%) between experiment and prediction at the stagnation point is disconcerting, and variations with fiber orientation angle and/or variation in recovery enthalpy made little or no difference in the predictions. This discrepancy remains to be resolved. The agreement between measurement and prediction is much better (between 2.5-5% difference) for the two plugs on the conical frustum.

Table 7. Comparison of measured and predicted surface temperatures

Plug location	Experiment (@t=25.s) °C	Computation (@t=25 s) °C	DT °C
Stagnation point	1670	2044	+335
Mid-cone	1521	1559	+38
Bottom cone	1402	1467	+65

Version 2.6.1 of FIAT permits analysis of sensitivity of materials response to variations in enthalpy. In the present work a ±10% variation (around the nominal) in enthalpy is considered. The predicted recession for the various cases is shown in Table 8. The results indicate a linear dependence of recession on enthalpy – a ±10% change in enthalpy yields a ±12% change in recession.

Table 8. Predicted recession using FIAT v2.6.1

	Stagnation Point Plug		Mid-cone Plug		Bottom-cone Plug	
	Recession in	Difference	Recession in	Difference	Recession in	Difference
0.9 Nom. enthalpy	0.1855	-10.8%	0.0658	-11.5%	0.0523	-11.9%
Nom. enthalpy	0.2079		0.0743		0.0594	
1.1 Nom. enthalpy	0.2305	10.8%	0.0829	11.5%	0.0664	11.9%

At the time of writing this report, detailed recession measurements had not been performed.

V. Conclusion

A fairly detailed analysis of AHF 295 has been completed, and results reported herein. After the test of SPRITE-T1-1, and upon preliminary examination of the condition of the tested article, it was decided to keep this small project in abeyance until all lessons learned are documented. From the perspective of simulation of arc-heated flows, one of the major accomplishments is the upgrade of the simulation process from one based on v3.05 to one based on v4.02.1 of DPLR. The upgrade led to a reduction in the number of free parameters, especially the inflow Mach number, in the simulation process. The internal consistency in calorimeter data led to the examination of the influence of both surface temperature and catalycity of copper. From the present effort, limited to just AHF 295, it appears that both issues need to be examined further, using either representative cases from other arc-jet tests in the same nozzle or further tests in the SPRITE program, to draw any definite conclusions. However, the lack of a calorimeter of the same size and shape as the SPRITE-T1 test article was acutely felt. A detailed examination of data acquired by the in-situ measurement capability remains, as does the analysis of the back shell environments (at least over the frustum).

Appendix

The preliminary flow field/materials response analysis of AHF 295 presented in the preceding section does not satisfactorily explain the observations of the test, at least without invoking assumptions about the temperature of the exposed face of the slug and the catalycity of copper, and clearly further study is needed. The four main issues from all the analysis performed thus far are:

(1) Is the surface temperature of 1073 K (800 °C) for the exposed face of the copper slug a tenable assumption, especially since the melting point of pure copper is roughly 1100 °C? At issue is the temperature recorded by the pyrometer, which is quite consistent with that recorded by the IR camera. However, the emissivity of polished copper is not close to unity. The net effect of raising the surface temperature from the value of 400 K used in the original simulation process is a net decrease in the predicted heat flux, but not enough to explain *all* calorimeter measurements in AHF 295. It is, however, possible to verify this assumption with numerical heat transfer analysis of the copper slug. The imposed (measured) heat flux on one end of the copper slug and thermal properties of copper can be used in a finite-element code such as *COMSOL* and the predicted time variation of the backface temperature can be compared against the experimental measurement. The sensitivity of the results to varying the surface temperature can then be examined.

(2) Is copper really partially non-catalytic? This assumption is tied in with the assumption of the surface temperature of the copper slug. If the surface temperature of the copper slug reaches very high temperatures, it is unlikely that the vibrating copper lattice (at a molecular level) will permit complete recombination of free atoms that diffuse to the surface.

(3) How accurate is the bulk enthalpy measurement, and how do the measurements in AHF 295 stack up against values in the facility database? Figure A1 shows a scatter plot of measured bulk enthalpy values (measurements by energy balance) as a function of the sonic flow parameter (Eq. 3). The sonic flow parameter depends only on the measured flow rates (of air and argon), and the arc column pressure. It is assumed that both these measurements are made reliably. Clearly there is a significant amount of scatter in the bulk enthalpy measurements. The bulk enthalpy measurements made in AHF 295 were reanalyzed and the original estimates, which varied between 11.1 and 13.5 MJ/kg, were revised to an average of 11.4 MJ/kg (see Table 1). The consistency in the revised measurement is encouraging. However, as is clearly seen in Fig. A1, the values measured in AHF 295 are significantly lower than those observed over the years in the same facility.

(4) The revised estimate of 11.4 MJ/kg (average) for the bulk enthalpy in AHF 295, and the estimated centerline enthalpy of 13.7 MJ/kg (average) from calorimeter measurements, suggest that there is an enthalpy profile. Past

scans of the free jet with a hemisphere-cylinder heat flux probe and a Pitot probe have not shown any variations of ±20% as is seen from measurements.

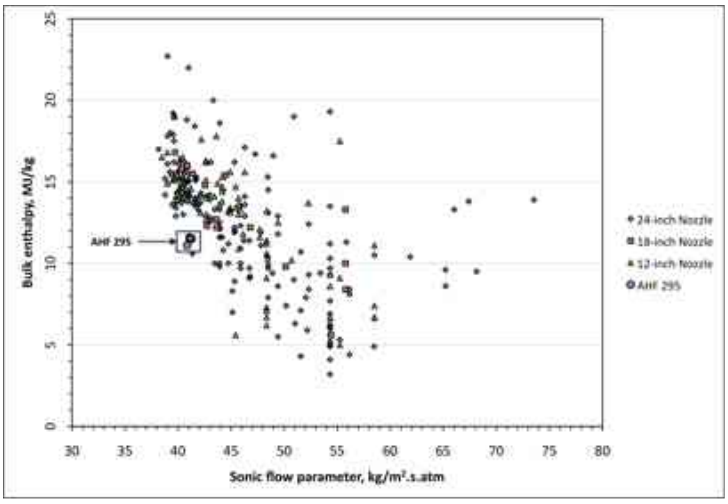

Figure A1. Measured enthalpies plotted as a function of the sonic flow parameter from several tests in the AHF. The size of the nozzle is not particularly meaningful in this context, unless the energy loss from the arc-heated stream is significant.

Assuming a reduced bulk enthalpy of 11.4 MJ/kg and uniform profiles for both enthalpy and mass flux, flow computations were performed again, only this time with the slug surface temperature set to 400 K and a fully catalytic wall assumption. The computed values of pressure and cold-wall heat flux at the stagnation point of each calorimeter are given in Table A1. Also shown in the table are the effective radii of each non-hemispherical calorimeter, using the 4-inch hemispherical calorimeter as the reference.

Table A1. Predictions of pressure & cold-wall heat flux at the stagnation point using *DPLR* v4.02.1

	Experiment			CFD (*DPLR* v4.02.1), H_{bulk} = 11.4 MJ/kg				
						Diff. from expt.		
Calorimeter	p_{stag} kPa	q_{stag} W/cm^2	R_{eff} in	p_{stag} kPa	q_{stag} W/cm^2	**Pressure**	**Ht. flux**	R_{eff} in
4in Hemi	8.28	222.0		8.02	217.4	-3.1%	-2.1%	
4in Iso-q	8.38	167.8	3.501	8.09	156.8	-3.5%	-6.6%	3.844
4in Flat Face	8.30	123.0	6.515	8.16	108.0	-1.7%	-22.0%	8.104
6in Flat Face	8.50	98.0	10.263	8.25	86.0	-2.9%	-22.4%	12.781

Whereas previously (see Table 4) with an assumed bulk enthalpy of 13.7 MJ/kg, the predicted heat fluxes for the hemispherical and iso-q were roughly 13-20% above the corresponding measurements, and the predicted heat fluxes for the flat-faced calorimeter were within 6% of corresponding measurements, the trend is the opposite with reduced enthalpy. With an assumed bulk enthalpy of 11.4 MJ/kg, the agreement between prediction and experiment is excellent for the calorimeters with surface curvature, but the agreement for the flat-faced calorimeters is bad (20-22% underprediction). Note: the reservoir/plenum pressure is the same for both the 13.7 and 11.4 MJ/kg computations. The distributions of surface pressure and cold wall heat flux for the various calorimeters are shown in Fig. A2.

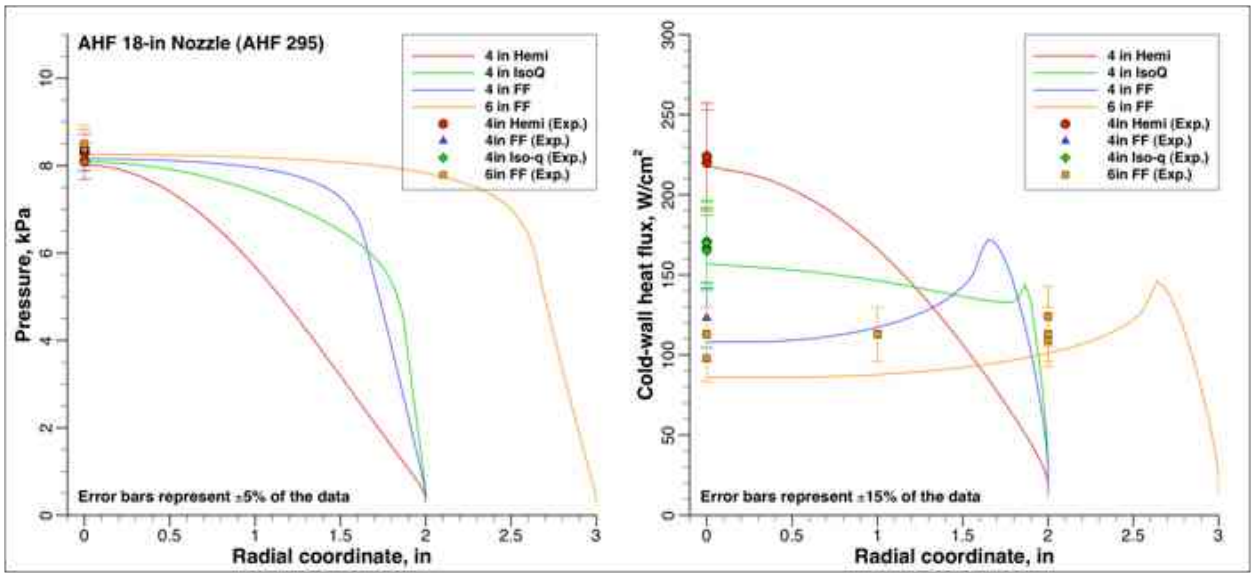

Figure A2. Time histories of predicted temperatures (surface and in-depth) from application of FIAT v2.6.1 to results from flow field computations.

Flow conditions used in calorimeter simulations are used in hot-wall simulations of the test article as well. As before, the computed flow field solution for the hot-wall case is post-processed using an in-house software utility, BLAYER, to extract boundary-layer properties – edge, wall, thickness, etc. The surface pressure, edge enthalpy, and convective heat transfer coefficient (film coefficient) are extracted at locations corresponding to the center of each instrumented plug (see Fig. 1). These quantities were provided as inputs to v2.6.1 of the materials thermal response code, FIAT. The predicted time histories of surface temperature, and in-depth temperatures corresponding to the thermocouple locations within the three instrumented plugs are shown Fig. A3.

Clearly, the assumption of a lower bulk enthalpy results in lower surface temperatures – decreases of the order of 100-150°C. Within the bulk material, the in-depth temperature decreases are of the order of 100 °C as well. Without a direct comparison against measured data, it is still difficult to draw any definitive conclusions other than to claim that the centerline enthalpy is closer to the 11.4 MJ/kg value rather than the 13.7 MJ/kg value inferred from calorimeter measurements.

Table A2. Comparison of measured and predicted surface temperatures

Plug location	Experiment (@t=25.s)	Computation (@t=25 s)	ΔT
	°C	°C	°C
Stagnation point	1670	1918	+248
Mid-cone	1521	1456	-65
Bottom cone	1402	1372	-30

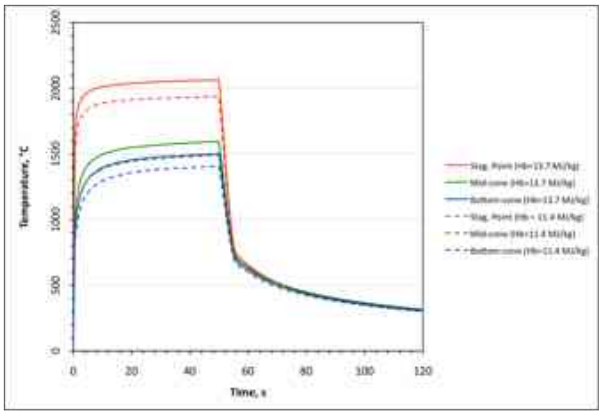

(a) Surface Temperature

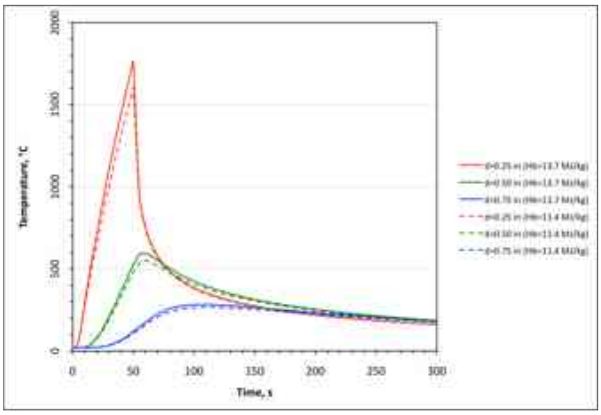

(b) TC response: Stagnation point

Acknowledgments

The author was supported by Contract NNA10DE12C to ERC Inc from the Entry Systems and Technology Division at NASA Ames Research Center, and by the goodwill of many programs and individuals interested in getting a better understanding of traceability of ground-based arc-jet testing to flight. The critical financial support provided by NASA-SCAP for the arc-jet operational capability at NASA Ames Research Center is gratefully acknowledged.

References

[1]Swanson, G., "Results and analysis of large scale article testing in the Ames 60 MW interaction heating arc jet facility," abstract submitted to the AIAA Aerospace Sciences Meeting, Nashville, TN, January 2011.

[2]Loomis, M. P., and Prabhu, D. K., "Results and analysis of large scale article testing in the Ames 60 MW interaction heating arc jet facility," abstract submitted to the AIAA Aerospace Sciences Meeting, Orlando, FL, January 2010.

[3]DS2 reference.

[4]Wright, M. J.,White, T. and Mangini, N., "Data-Parallel Line Relaxation Methods (DPLR) Code User Manual Acadia-Version 4.01.1," NASA/TM-2009-215388, October 2009.

[5]Chen, Y.-K., and Milos, F. S., "Ablation and Thermal Response Program for Spacecraft Heatshield Analysis," *Journal Spacecraft and Rockets*, Vol. 36, No. 3, 1999, pp. 475-483.

[6]MSC Software Corporation, 2 MacArthur Place, Santa Ana, CA 92707.

[7]Thermal Desktop reference????

[8]Fay, J. A., and Riddell, F. R., "Theory of Stagnation Point Heat Transfer in Dissociated Air," *Journal of Aeronautical Sciences*, Vol. 25, No. 2, 1958, pp. 73-85.

[9]Zoby, E. V., "Empirical Stagnation-Point Heat-Transfer Relation in Several Gas Mixtures," NASA TN D-4799, Oct. 1968.

[10]Zoby, E. V., and Sullivan, E. M., "Effects of Corner Radius on Stagnation-Point Velocity Gradients on Blunt Axisymmetric Bodies," Journal of Spacecraft and Rockets, Vol. 3, No. 10, pp. 1567-1567, 1966.

[11]Hightower, T. M., Balboni, J. A., MacDonald, C. L., Anderson, K. F., and Martinez, E. R., "Enthalpy by Energy Balance for Aerodynamic Heating Facility at NASA Ames Research Center Arc Jet Complex," 48th International Instrumentation Symposium, The Instrumentation Systems, and Automation Society, Research Triangle Park, NC, May 2002.

[12]Winovich, W., "On the equilibrium sonic flow method for evaluating electric-arc air-heater performance," NASA TN D-2132, March 1964.

[13]Shepard, C. E., Milos, F. S., and Taunk, J. S., "A sonic flow equation for electric arc jets," AIAA Paper 1993-3183, July 1993.

[14]Thompson, C. S., Prabhu, D., Terrazas-Salinas, I., and Mach, J. J., "Bulk enthalpy calculations at NASA ARC Arc Jet Facility," abstract submitted to the 42nd AIAA Thermophysics Conference, Honolulu, HI, 2011.

[15]Prabhu, D K, et al., CFD Analysis Framework for Arc-Heated Flowfields, I: Stagnation Testing in Arc-jets at NASA ARC, AIAA Paper AIAA-2009-4080, June 2009.

[16]Saunders, D. and Gökçen, T., "Nozzle Throat Conditions for Arc-jet Computations (1) Axisymmetric," ELORET Report TSA-01-DB2-1-2008, October 2008.

[17]Gordon, S., and McBride, B. J., "Computer program for calculations of complex chemical equilibrium compositions, rocket performance, incident and reflected shock, and Chapman-Jouguet detonations," NASA/SP-273, 1976.

[18]Davies, C. B., and Venkatapathy, E., "SAGE: The Self-Adaptive Grid CodE," NASA/TM-1999-208792, August 1999.

[19]Barbato, M., Reggiani, S., Bruno, C., and Muylaert, J., "Model for Heterogeneous Catalysis on Metal Surfaces with Applications to Hypersonic Flows," *Journal of Thermophysics and Heat Transfer*, Vol. 14, No. 3, 2000, pp. 412-420.